Science and Technology of Advanced Materials

ISSN: 1468-6996 (Print) 1878-5514 (Online) Journal homepage: www.tandfonline.com/journals/tsta20

Optimization of thermoelectric performance in Sm-substituted $SrSi_2$ via carrier transport and lattice engineering

Vikrant Trivedi, Naohito Tsujii & Takao Mori

To cite this article: Vikrant Trivedi, Naohito Tsujii & Takao Mori (2025) Optimization of thermoelectric performance in Sm-substituted $SrSi_2$ via carrier transport and lattice engineering, Science and Technology of Advanced Materials, 26:1, 2551486, DOI: 10.1080/14686996.2025.2551486

To link to this article: https://doi.org/10.1080/14686996.2025.2551486

SCIENCE AND TECHNOLOGY OF ADVANCED MATERIALS
2025, VOL. 26, NO. 1, 2551486
https://doi.org/10.1080/14686996.2025.2551486

Taylor & Francis
Taylor & Francis Group

FOCUS ISSUE ARTICLE

OPEN ACCESS Check for updates

Optimization of thermoelectric performance in Sm-substituted $SrSi_2$ via carrier transport and lattice engineering

Vikrant Trivedi [a], Naohito Tsujii [a] and Takao Mori [a,b]

[a]Research Center for Materials Nanoarchitectonics (MANA), National Institute for Materials Science (NIMS), Tsukuba, Japan;
[b]Graduate School of Pure and Applied Sciences, University of Tsukuba, Tsukuba, Japan

ABSTRACT

The pursuit of sustainable thermoelectric materials requires the development of cost-effective and efficient compounds derived from earth-abundant elements. Here, we investigate the effects of samarium (Sm) substitution on the thermoelectric performance of $SrSi_2$ with compositions $Sr_{1-x}Sm_xSi_2$ ($x = 0$, 0.05, 0.1, 0.15, and 0.2). Substituting Sm for Sr in $SrSi_2$ enhances the power factor at low substitution levels, while further substitution leads to a decrease, due to increased carrier scattering and reduced Seebeck coefficient. Introducing Sm substitution enhances phonon scattering through point defects, reducing lattice thermal conductivity. A peak figure of merit (ZT) of ~0.23 at room temperature is achieved for $Sr_{0.95}Sm_{0.05}Si_2$, demonstrating a 35% improvement over undoped $SrSi_2$. The weighted mobility of ~285 $cm^2/V{\cdot}s$ and the tailored thermal transport emphasize the role of Sm substitution in modulating both electronic and thermal properties. These findings establish $Sr_{1-x}Sm_xSi_2$ as a promising candidate for next-generation thermoelectric devices.

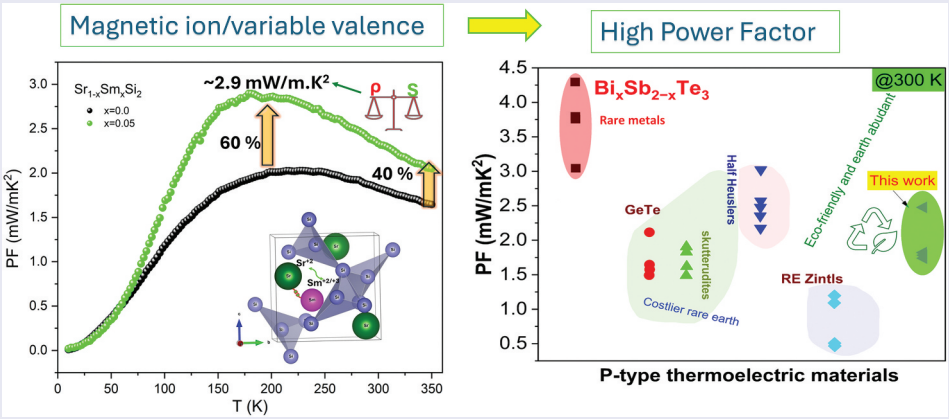

ARTICLE HISTORY
Received 24 April 2025
Accepted 19 August 2025
Revised 23 July 2025

KEYWORDS
Thermoelectric material; silicide; seebeck coefficient; electrical resistivity; thermal transport

IMPACT STATEMENT

A high p-type thermoelectric power factor of 2.9 mW/K^2m and $ZT = 0.23$ was achieved around room temperature by incorporating the mixed-valent Sm^{2+}/Sm^{3+} ion to the earth-abundant and environmentally friendly material $SrSi_2$.

1. Introduction

The urgent need for developing renewable energy sources is more pressing than ever. Thermoelectric (TE) materials that can directly convert heat into electricity are crucial for energy harvesting and solid-state cooling technologies. This conversion relies on the movement of charge carriers and phonons. It offers several advantages, including minimal noise, no pollution, low maintenance requirements, and a long operational lifespan [1].

The effectiveness of a thermoelectric device in generating power or providing cooling is defined by the dimensionless figure of merit ZT ($ZT=S^2T/\kappa\rho$) of the materials. In this formula, T represents the absolute temperature, and S^2/ρ is the power factor, where S is the Seebeck coefficient, ρ is the electrical resistivity, and κ is the thermal conductivity, in which the electron and phonon contributions are involved. Suitable thermoelectric materials must have significant Seebeck coefficient,

CONTACT Naohito Tsujii TSUJII.Naohito@nims.go.jp; Takao Mori MORI.Takao@nims.go.jp Research Center for Materials Nanoarchitectonics (MANA), National Institute for Materials Science (NIMS), Namiki 1-1, Tsukuba 305-0044, Japan
Supplemental data for this article can be accessed online at https://doi.org/10.1080/14686996.2025.2551486

high electrical conductivity, and low thermal conductivity. Practical thermoelectric materials have typical ZT values around 1. In recent decades, there has been renewed interest in finding new materials with excellent thermoelectric properties. These materials include rare-earth-filled skutterudites [2–4], MgAgSb [5], Mg_3Sb_2 [6–8], half-Heuslers [9]. Thus, the development of high-performance thermoelectric materials with earth-abundant and environmental-friendly elements is the current requirement.

Recently, alkaline-earth-metal disilicides have gained attention because they consist of non-toxic and naturally abundant elements. $SrSi_2$ is recognized as a narrow-gap semiconductor, featuring a band gap of approximately 35 meV [10]. It may also be classified as a topological Weyl semimetal, as inferred by the band structure calculations [11,12]. Despite this understanding, literature on enhancing its thermoelectric properties is scarce. $SrSi_2$ has two main phases: a cubic phase (α) that occurs at low temperatures and a tetragonal phase (β) that appears at high temperatures. The transition between these phases happens between 700 and 800 K. Theoretical calculations show that tetragonal β-$SrSi_2$ has a metallic character, while α-$SrSi_2$ has a band gap in the near-infrared range, making it useful for detecting infrared rays in silicon devices [13,14]. Achieving phase-pure α-$SrSi_2$ is typically challenging, and the presence of residual impurities can significantly influence the thermoelectric properties. For instance, α-$SrSi_2$ has been reported to exhibit a power factor (S^2/ρ) ranging from approximately 1.6 to 2.4 mW/m·K^2 at 300 K, depending on synthesis methods and microstructural modifications, with some values approaching those of commercial Bi_2Te_3-based thermoelectric materials [12,15,16]. The power factor (PF) of various doped $SrSi_2$ compositions exhibits notable improvements due to their high electrical conductivity and Seebeck coefficient. However, the material maintains a relatively high thermal conductivity of 5 to 6 W/m·K at room temperature [17]. The high thermal conductivity of pure α-$SrSi_2$ results in a moderate dimensionless figure of merit (0.05–0.15) at room temperature. Nevertheless, α-$SrSi_2$ is recognized for having the highest ZT among p-type silicides at room temperature. DFT calculations suggest an optimal ZT of approximately 0.77 at 300 K and nearly 1 at 50 K [18]. Hence, further optimization of thermoelectric properties is necessary. Several strategies were earlier applied in the case of α-$SrSi_2$ by doping iso-electronic atoms (Ca, Ba, and Ge), electron and hole doping on Sr and Si sites (Y and Al), and processing techniques for nanostructuring (ball milling and melt spinning) [19]. Nanostructuring and doping are the most effective methods for optimizing phonon scattering in the lattice, reducing thermal conductivity without affecting the power factor.

In this study, we rigorously explore the impact of Sm substitution on the thermoelectric properties of $SrSi_2$. Since Sm has a larger atomic size, its addition may significantly affect thermal conductivity due to mass/strain fluctuations. Also, replacing Sr with Sm could modify the band structure, as Sm has an extra electron in its valence shell compared to Sr. Furthermore, rare-earth elements such as Ce, Sm, Eu, and Yb may sometimes show valence instability because of dual-valence states (Ce^{3+}/Ce^{4+}, Sm^{2+}/Sm^{3+}, Eu^{2+}/Eu^{3+}, Yb^{2+}/Yb^{3+}). In that case, it potentially brings the Fermi level closer to a sharp peak in the density of states (DOS) [20–24]. Additionally, Sm, a magnetic ion, can generate magnetic entropy to enhance the Seebeck coefficient due to the degeneracy of its electronic structure [25]. We thus investigated the effect of Sm substitution in $SrSi_2$, namely, $Sr_{1-x}Sm_xSi_2$ ($x = 0$, 0.05, 0.1, 0.15, and 0.2) on the thermoelectric properties. This study provides a pathway for leveraging the dual-valence characteristics of rare-earth ions in $SrSi_2$, potentially enhancing its thermoelectric properties.

2. Experiments

2.1. Sample preparation

The samples of the polycrystalline $Sr_{1-x}Sm_xSi_2$ (where $x = 0$, 0.05, 0.1, 0.15, and 0.2) were prepared using the Ar arc melting, ball milling, and spark plasma sintering route. For starting materials, Sr (3N, Furuuchi chemical, chunk), Sm (3N, Furuuchi chemical, chunk), and Si (10N, Furuuchi chemical, chunk) were used. The starting materials were placed in a water-cooled copper hearth under an argon atmosphere in the arc furnace. Multiple melting cycles were carried out to ensure homogeneity. To maintain the correct stoichiometry, an additional amount of Sr was added to compensate for its evaporation during the arc-melting process.

The arc-melted ingots were crushed in a WC-lined mortar pestle and ball-milled under an Ar atmosphere using a WC grinding medium by a planetary ball mill (Pulverisette-6, Fritsch, Germany) at a speed of 300 rpm for 3 hours. The milled powders were loaded in a graphite die under an Ar glove box and pelletized by the spark plasma sintering (SPS) with an SPS-1080 (Syntex Inc., Japan) at 1073 K and 80 MPa uniaxial pressure for 15 min in a static vacuum (2×10^{-2} Pa).

2.2. Sample characterization

Powder X-ray diffraction was measured using a RINT TTR-3 diffractometer (Rigaku Co., Akishima, Tokyo, Japan) with Cu K_α radiation. The diffraction data were refined using the Rietveld method through FullProf Suite, with Si (NIST 640d) employed as an external

standard [26]. SEM and Electron backscattered diffraction (EBSD) measurements were performed using a FE-SEM (JSM-7001F, JEOL Ltd.). The EBSD measurements were done at 15 kV with a step size of 0.2 μm. The EBSD sample preparations were done by mechanical polishing to 0.1 μm with diamond paste and then ion milling. Chemical compositions were evaluated by using energy dispersive spectroscopy (EDS). X-ray photoelectron spectroscopy (XPS) measurements were conducted in a UHV system using a PHI 5000 VersaProbe II spectrometer (ULVAC-PHI, Japan). The thermoelectric properties ρ, S, and κ data were measured at temperatures ranging from 10 to 350 K using a Physical Property Measurement System (PPMS, Quantum Design) with the Thermal Transport Option (TTO) and the four-probe method. Bar-shaped samples with typical dimensions of 3 mm × 3 mm × 10 mm were used for these measurements. Corrections were made for heat loss due to radiation effects and dissipation through the leads to account for thermal conductivity data. The detailed procedure is documented elsewhere [27]. The room temperature Hall resistivity $\rho_{xy}(H)$ was measured under a magnetic field H ranging from −7 T to + 7 T at intervals of 1 T. The Hall coefficient (R_H) was evaluated from the least-squares fitting of the antisymmetric part of $\rho_{xy}(H)$, $[\rho_{xy}(+H) - \rho_{xy}(-H)]/2$, against H to exclude the longitudinal contribution due to a possible misalignment of the Hall contacts. The carrier concentration and mobility were derived by $n_H = 1/(eR_H)$ and $\mu_H = R_H/\rho$, respectively. The measurement uncertainties were primarily based on the TTO system specifications. The typical accuracy for thermal conductivity (κ) is within ± 5% or the minimum detection limit, depending on the temperature range. The Seebeck coefficient (S) uncertainty is ± 5%, ±0.5 μV/K, or ±2 μV in voltage, whichever is greater. While the precision of resistivity (ρ) measurements is typically better than 0.01% for a resistance of 1 Ω at a measurement current of 200 μA, the overall uncertainty in ρ is predominantly governed by errors in measuring sample dimensions and contact area. These geometric uncertainties are estimated to result in an overall ± 5% error in resistivity. The uncertainty in the calculated thermoelectric figure of merit (ZT) is estimated to be ± 20%, assuming ± 5% errors in κ, S, and resistivity (ρ), with negligible contribution from temperature measurement errors. Error bars have been added to the relevant figures for clarity; these uncertainties were carefully considered during the analysis and interpretation of the thermoelectric performance.

3. Results and discussion

3.1. Phase formation and microstructure evolution

Figure S1 (a, b) and Figure 1(a) show the powder X-ray diffraction (XRD) patterns of the Ar arc-melted, ball-milled, and SPSed samples in the range of $10° \leq 2\theta \leq 80°$, respectively. Each XRD result can be indexed to match the space group $P4_332$ (No. 212). The XRD patterns of ball-milled powders in Figure S1(b) suggest that nanostructuring and disordering occurred due to ball milling, as evidenced by the broad XRD peaks. However, even after SPS, all the samples contained a minor portion of the tetragonal β-phase. The lattice parameter of the SPSed samples was estimated through Rietveld refinement of the XRD pattern (Figure 2(a,b)), which is plotted in Figure 1(b) as a function of the Sm concentration. The lattice parameter increases linearly with x, indicating that Sm atoms effectively replace Sr. The XRD data were further analyzed using a modified Williamson-Hall (W-H) method to estimate crystallite size, dislocation density, and lattice strain. Further details are available in the supporting

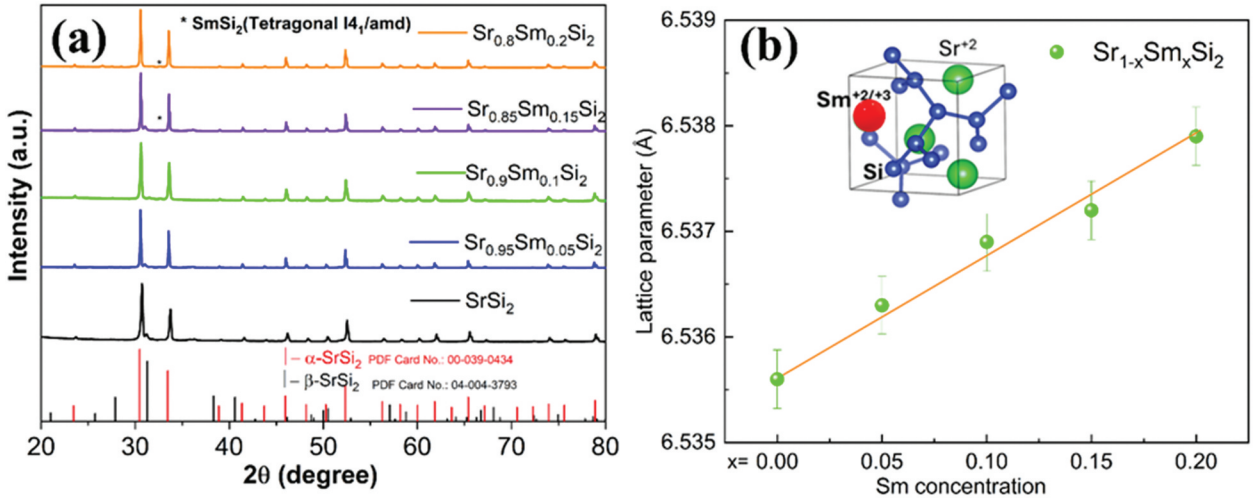

Figure 1. X-ray diffraction pattern of (a) SPSed $Sr_{1-x}Sm_xSi_2$ samples with the peak corresponding to the α-$SrSi_2$ and β-$SrSi_2$ phases, impurity peaks at $x = 0.15$ and 0.2, marked by asterisks. (b) Lattice constant as a function of Sm content in $Sr_{1-x}Sm_xSi_2$ samples. The inset in panel (b) illustrates the crystal structure of α-$SrSi_2$.

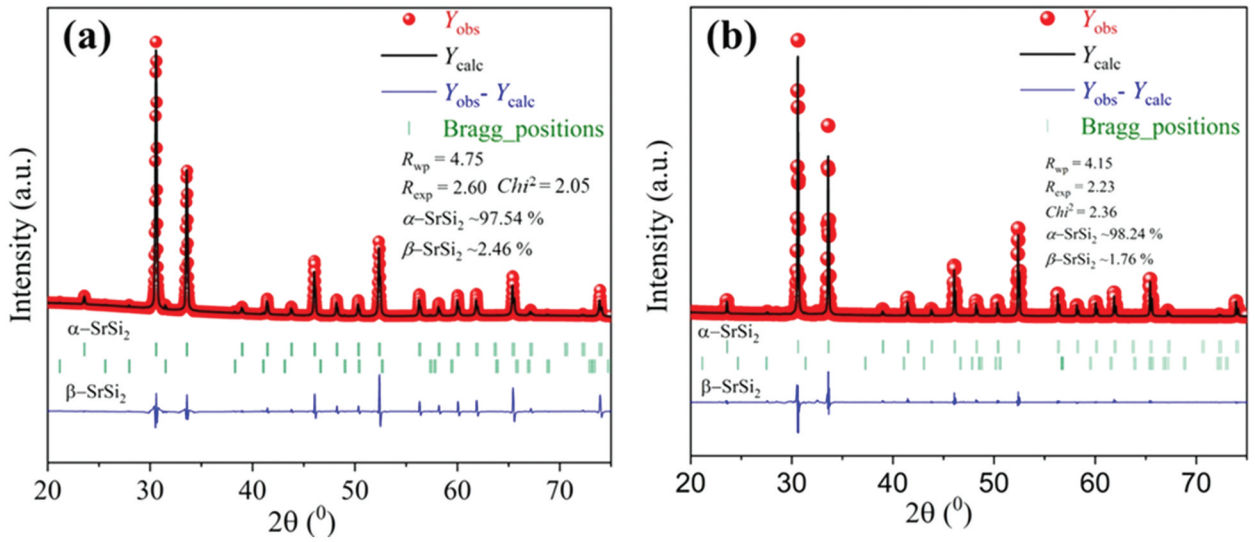

Figure 2. (a-b) XRD patterns of $SrSi_2$ and $Sr_{0.95}Sm_{0.05}Si_2$ SPSed samples with the Rietveld refined results and phase fractions.

information file. Figure S1(c) shows the average values of the samples' dislocation density and crystallite size.

We performed scanning electron microscopy with energy-dispersive X-ray spectroscopy (SEM-EDS) on the polished and fractured surfaces of $Sr_{1-x}Sm_xSi_2$ to investigate the sample composition and morphology. Figures S2(a) and S3(a) present backscattered electron images (BEI) of arc-melted $SrSi_2$ and $Sr_{0.85}Sm_{0.15}Si_2$ samples, revealing three distinct regions: light, dark, and black. Elemental mapping of the arc-melted sample, as shown in Figures S2(b-c), indicates that the light areas correspond to the primary $SrSi_2$ phase. In Figure S3(b-d), the white regions represent the Sm-rich impurity phase, while the gray and black regions are identified as the primary $SrSi_2$ phase. Figures 3(a,e) display SEM images of fractured surfaces of two SPSed $SrSi_2$ and $Sr_{0.95}Sm_{0.05}Si_2$. The images reveal dense samples (~98% relative density) with no noticeable porosity. In Figures 3(b,f), the polished surfaces of the samples appear homogeneous, with no observable precipitated phases. Figures 3(c,d,g–i) show the EDS mapping of Sr, Sm, and Si for the SPSed $SrSi_2$ and $Sr_{0.95}Sm_{0.05}Si_2$ samples. These mappings confirm that all elements are uniformly distributed. Figure S4 shows BEI images of SPSed $Sr_{0.85}Sm_{0.15}Si_2$ S4(a) and $Sr_{0.8}Sm_{0.2}Si_2$ S4 (e). The lighter regions indicate a significant presence of Sm-rich secondary phases, as seen in the XRD analysis. EDS analysis results (Table 1) demonstrate that the primary elements in the samples match their nominal compositions.

EBSD analysis was performed on undoped $SrSi_2$ and Sm-substituted ($x = 0.05$) samples to study the

Table 1. Energy-dispersive X-ray spectroscopy (EDS) results of $Sr_{1-x}Sm_xSi_2$ SPSed samples, showing nominal vs actual composition of samples.

$x_{Nominal}$	Sr (at. %)	Sm (at. %)	Si (at. %)	x_{Actual}
0.00	32.7	–	67.3	0.00
0.05	30.6	2.1	67.2	0.07
0.10	29.6	3.1	67.3	0.09
0.15	29.1	4.0	66.9	0.12
0.20	26.9	6.2	66.9	0.19

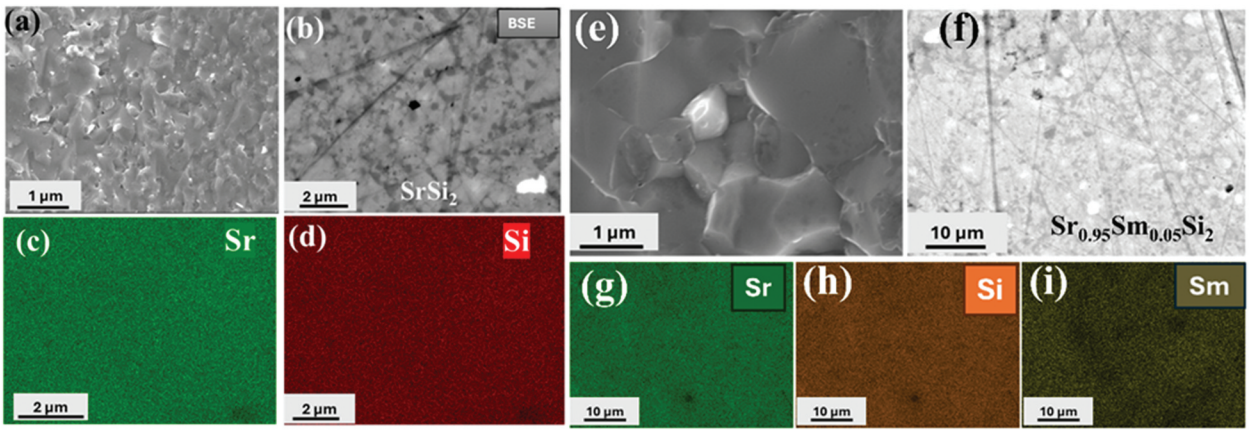

Figure 3. SEM image at the fractured surface of $SrSi_2$ (a) and $Sr_{0.95}Sm_{0.05}Si_2$ (e). BSE images at the polished surfaces of SPSed $SrSi_2$ (b) and $Sr_{0.95}Sm_{0.05}Si_2$ (f), and the respective EDS elemental mapping (c, d) for $SrSi_2$ and (g-i) for $Sr_{0.95}Sm_{0.05}Si_2$ (f).

effect of Sm substitution on local crystallography. Figure 4 shows orientation maps with colors representing Miller indices. Black spots signify unresolved areas caused by higher local strains or surface porosity that were excluded from the analysis. The Euler images (Figure 4(a,c)) reveal well-crystallized, randomly oriented grains. The grain size histograms (Figure 4(b,d)) indicate an increase in the average grain size from 400 ± 25 nm for $SrSi_2$ to 1.3 ± 0.4 μm for $Sr_{0.95}Sm_{0.05}Si_2$, which is likely a result of Sm substitution influencing grain boundary mobility and crystallization kinetics, as rare-earth doping has been reported to reduce grain boundary mobility through solute drag and lattice strain effects [28]. However, grain size variation and the inability of EBSD to distinguish sub-grains separated by low-angle boundaries must be considered [29].

Figure 5 illustrates local misorientation angles between adjacent grains and Kernel Average Misorientation (KAM) plots, providing insights into lattice distortions and dislocation density. High KAM values, particularly near grain boundaries, indicate significant dislocation density [30]. As discussed below, microstructural features like grain size, misorientation, and dislocation density critically impact thermoelectric performance by balancing enhanced phonon scattering with preserved electrical conductivity.

3.2. Thermoelectric properties

3.2.1. Electrical resistivity

The temperature-dependent electrical resistivity (ρ) for $Sr_{1-x}Sm_xSi_2$ ($0.0 \leq x \leq 0.2$) is presented in Figure 6(a). The substitution of Sm for Sr reduces the electrical

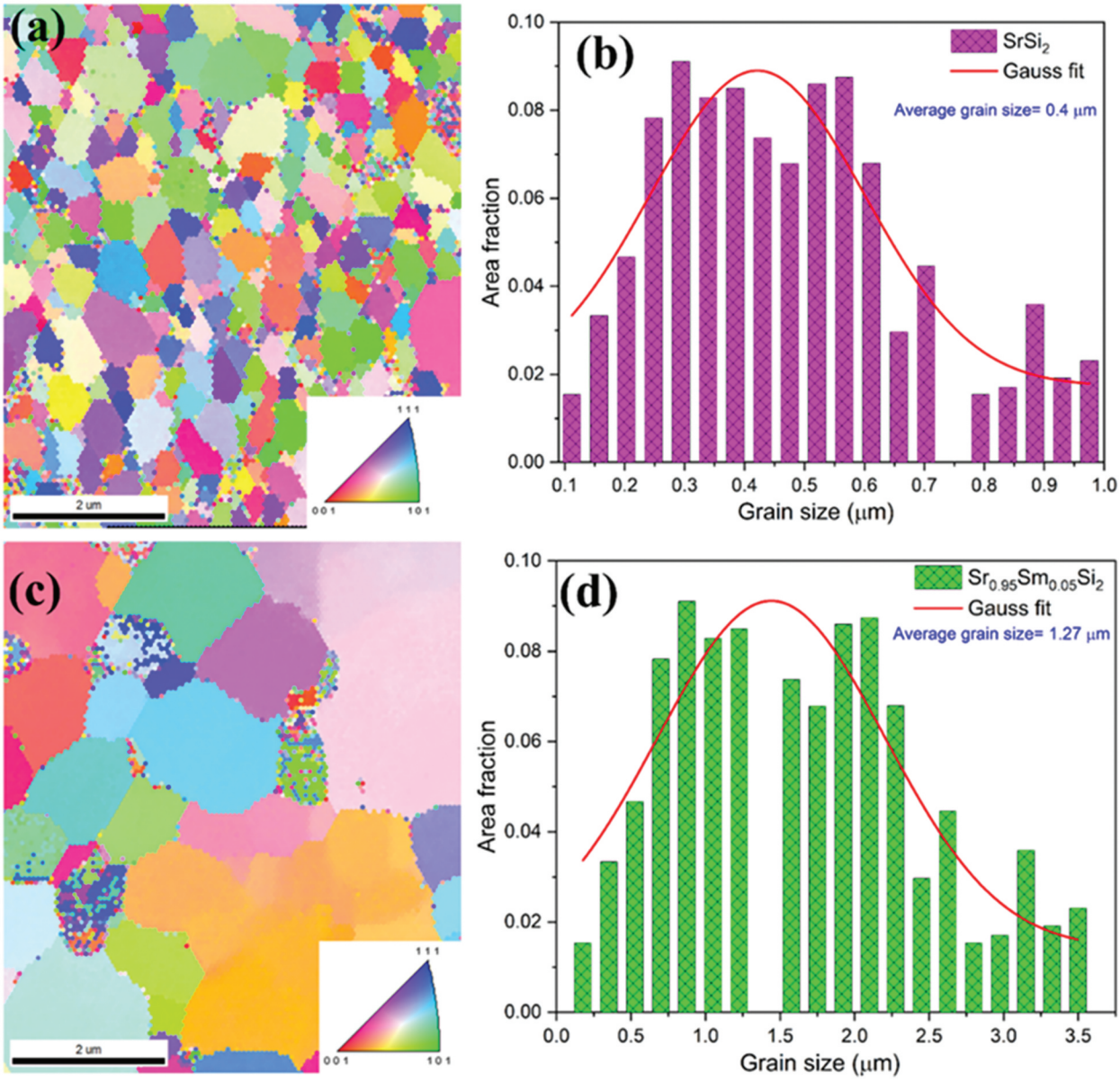

Figure 4. Electron backscatter diffraction (EBSD) patterns and grain size distribution for the undoped $SrSi_2$ and $Sr_{0.95}Sm_{0.05}Si_2$ samples. (a, c) and (b, d) are Euler images and histograms of the grain size of $SrSi_2$ and $Sr_{0.95}Sm_{0.05}Si_2$ samples, respectively. The insets in (a) and (c) are color-coded inverse Pole images.

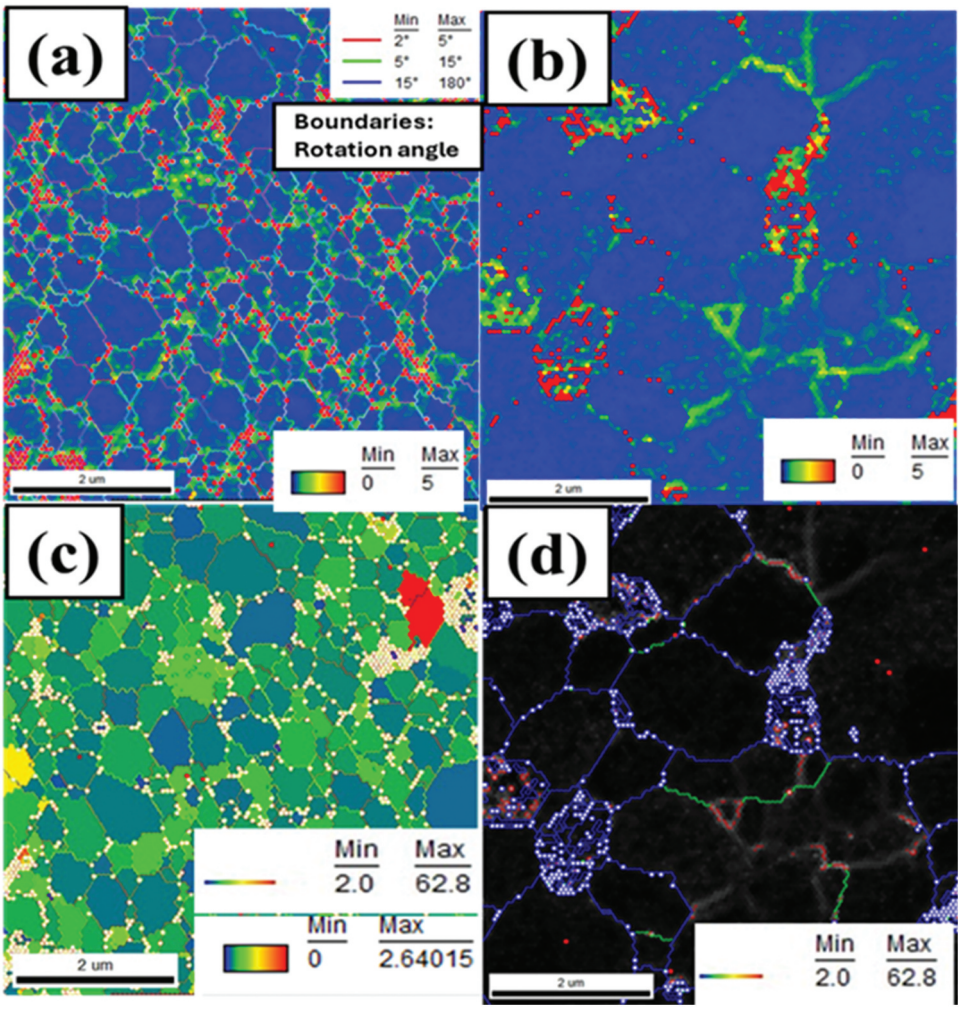

Figure 5. EBSD results of kernel average misorientation (KAM) maps of (a) $SrSi_2$ and (b) $Sr_{0.95}Sm_{0.05}Si_2$ sample, EBSD measured KAM plots of the sample showing higher dislocation density near the low angle boundaries. (c, d) grain boundary maps with grain orientation spread. In (c, d), color-coded grain boundaries with local misorientation angles are classified into several angular ranges.

resistivity. The room temperature electrical resistivity is lower than reported in the previous literature [19,31,32]. All samples show a negative temperature coefficient of resistivity below 180 K. It has been observed that the room-temperature resistivity first decreases for Sm content up to $x = 0.10$ before increasing with further substitution. Room-temperature resistivity (ρ_{RT}) of the $Sr_{0.95}Sm_{0.05}Si_2$ was found to be decreased to (~6.23 μΩ.m) from that of undoped $SrSi_2$ (~8.70 μΩ.m). In the case of $Sr_{0.8}Sm_{0.2}Si_2$, the absolute value of electrical resistivity increased, which suggested the effect of optimum electron doping and the role of secondary phases. The presence of secondary metallic phases such as β-$SrSi_2$ and $SmSi_2$ in the sample can lead to an increase in the overall electrical resistivity despite their intrinsic metallic nature [33,34]. This counterintuitive behavior arises primarily from enhanced electron scattering at the interfaces between the primary thermoelectric matrix and the metallic inclusions. These secondary phases typically form incoherent or semi-coherent boundaries with the host matrix, which act as scattering centers for charge carriers. The resulting carrier scattering, both elastic and inelastic, disrupts the charge transport pathways, thereby increasing resistivity. Additionally, compositional and structural inhomogeneities introduced by the impurity phases can lead to potential barriers or localized states, further hindering carrier mobility [35]. Thus, even though β-$SrSi_2$ and $SmSi_2$ are metallic, their dispersion within the matrix contributes to resistivity enhancement due to interfacial scattering effects and disruption of carrier percolation pathways. The increase in the absolute value of resistivity confirms a typical extrinsic behavior of metal/semi-metal. Imai et al. [10] also noted a decrease in electrical resistivity from 30 to 370 K, followed by a slight increase, which aligns closely with our results. Hashimoto et al. [32] and Aoyama et al. [36] also observed similar trends in samples made from commercial $SrSi_2$ chunks. Similarly, as Singh et al. showed, replacing Sr with a larger atomic radius, which would induce a negative chemical pressure in the system, can alter the band characteristics [15]. The band gap of the samples at semiconducting temperature regions was calculated by fitting the ρ–T data employing

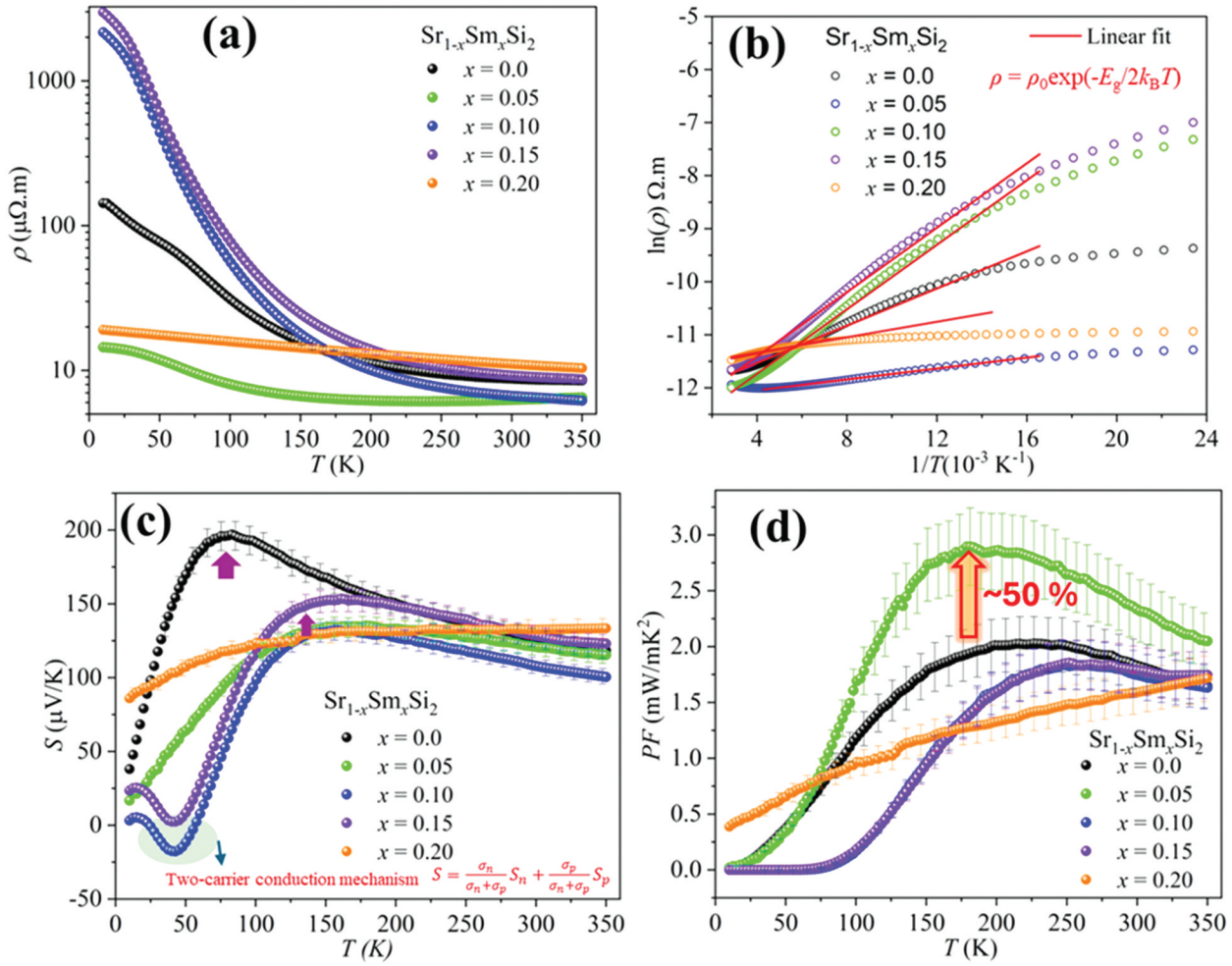

Figure 6. (a) Temperature dependence of electrical resistivity $\rho(T)$ for $Sr_{1-x}Sm_xSi_2$. (b) ln(ρ) vs 1/T. Solid red lines represent the fitting to the equation $\rho = \rho_0 \exp(-E_g/2k_BT)$, where ρ_0 is a constant, E_g is the band gap, and k_B is the Boltzmann constant. (c) Seebeck coefficient (S) and (d) power factor (PF) of $Sr_{1-x}Sm_xSi_2$ samples. The estimated relative error in PF is ± 15%, while the estimations of S and ρ have errors of ± 5%, as indicated by the representative error bar in figures.

the Arrhenius equation $\rho = \rho_0 \exp(-E_g/2k_BT)$, where ρ_0 is a constant, E_g is the band gap, and k_B is the Boltzmann constant. The experimental data were analyzed by fitting into a linear equation involving ln(ρ) and 1/T, shown in Figure 6(b). E_g for undoped $SrSi_2$ was obtained as 25 meV, consistent with the previous literature [11,15,32]. The value of E_g increases for lower Sm content ($x = 0.05$, 0.1) and decreases for higher Sm substitution levels ($x = 0.15$, 0.2) (see Table 2), suggesting the system became more metallic when doped heavily. Additionally, the presence of mixed-valence Sm^{2+}/Sm^{3+} may not only influence carrier concentration but could also induce cooperative structural distortions or local symmetry changes within the lattice. While such changes may not be easily detected by conventional XRD due to their subtle or short-range nature, they could still impact the electronic structure and transport behavior [20,22]. To further investigate the possible valence states of Sm, we performed X-ray photoelectron spectroscopy (XPS) measurements for samples with $x = 0.05$ and $x = 0.15$. These measurements help clarify the presence of mixed-valence Sm^{2+}/Sm^{3+} and their potential role in influencing both the electronic structure and local environment of the host lattice (Figures S5 and S6). The results agree with previous reports (see ESI) [37]. Due to a slight difference in the binding energies of Sm^{2+} and Sm^{3+}, it was only possible to qualitatively deconvolute the peaks.

Table 2. Band gap (E_g), resistivity (ρ) at 10 K, 300 K, carrier concentration (n_H), carrier mobility (μ_H), and the temperature at which S has a maximum value.

x	E_g (meV)	ρ_{10K} (μΩ.m)	ρ_{300K} (μΩ.m)	n_H (10^{20} cm^{-3})	μ_H(cm^{2}V^{-1}s^{-1})	T^S_{max} (K)
0.00	25.8	142.2	8.7	0.96	73.6	85.5
0.05	31.5	14.4	6.2	1.04	99.6	181.2
0.10	24.4	2165	6.4	1.25	74.8	158.5
0.15	23.6	2988	9.1	0.33	201.9	163.6
0.20	23.1	19.05	11.02	0.18	308.0	163.6

Therefore, within the scope of this work, determining the exact ratio of Sm^{2+}/Sm^{3+} is not feasible.

Nevertheless, these resistivity trends align with Kuo et al. [31] and Shiojiri et al. [11], who state that the metallic behavior of highly doped samples at high temperatures may be due to impurities and defects. We also performed ball-milling to make fine powders, as that process is also known for generating defects like dislocations. Figure 5 shows that higher KAM values near grain boundaries and misoriented grains often indicate a greater defect density. Interestingly, the electrical resistivity is highly sensitive to defects known as scattering centers [38,39]. These observations indicate that the effects of variable valence state, along with secondary phases and tailored microstructure, play a crucial role in the band characteristics of Sm-substituted $SrSi_2$, as indicated also by band structure calculations [11,14].

3.2.2. Seebeck coefficient, power factor, and weighted mobility

The temperature dependence of the Seebeck coefficient (S) of $Sr_{1-x}Sm_xSi_2$ SPSed samples is shown in Figure 6(c). The positive sign of S indicates that hole-type carriers are dominant, consistent with a small hole pocket near the Fermi level [40]. For each composition, the Seebeck coefficient shows a broad maximum below 150 K, a usual feature arising from thermally excited electrons moving across the gap or pseudo gap [41,42]. Doping induces a higher temperature shift in the broad maximum of S upon increasing Sm. The room-temperature value of S ~135 μV/K for $SrSi_2$ is consistent with the previous reports [15,32,41]. The absolute S decreased with increasing temperature, probably due to the increase of carriers by thermal excitation [11,19]. It is also worth mentioning that substituted semiconductors obey a two-carrier conduction mechanism. Accordingly, the total S can be expressed as

$$S = \frac{\sigma_n}{\sigma_n + \sigma_p} S_n + \frac{\sigma_p}{\sigma_n + \sigma_p} S_p \quad (1)$$

$S_{n,p}$ and $\sigma_{n,p}$ represent the Seebeck coefficients and electrical conductivities for the n- and p-type carriers. Subsequently, the signs of S_n and S_p are opposite, as governed by electron and hole transport. In the case of narrow-gap semiconductors or semimetals, thermal excitation of charge carriers can lead to the bipolar effect. For $x = 0.10$ and 0.15, the low-temperature Seebeck coefficient is negative, with peaks observed around 50 K, which can be qualitatively attributed to two-carrier conduction. As shown in Figure 6(c), the Sm-substituted samples exhibit dominant n-type carriers at low temperatures due to electron doping. At higher temperatures (above 100 K), the transport properties gradually become dominated by holes, most likely because the hole mobility is higher than that of electrons, as similarly reported in Y-substituted $SrSi_2$ systems by Lue et al. [17]. However, it is important to note that the samples with higher Sm content ($x \geq 0.10$) contain significant metallic secondary phases such as β-$SrSi_2$ and $SmSi_2$, which may contribute to the observed electrical transport. Therefore, the explanation based solely on intrinsic doping and bipolar effects is not sufficient, and the complex multi-phase nature of these samples must be considered when interpreting the transport behavior.

To gain deeper insight into the electrical transport properties, room-temperature carrier concentration and mobility were measured as a function of Sm content in $Sr_{1-x}Sm_xSi_2$, as shown in Figure 7(c) and Table 2. The samples demonstrate higher carrier concentrations than those previously reported in the literature [10,16]. This difference is likely due to variations in synthesis routes, Sr deficiency confirmed by EDS, and the presence of metallic secondary phases, all of which can influence the effective carrier density. Additionally, the grain size difference between the undoped (~400 nm) and Sm-substituted (~1.5 μm) samples suggests that grain boundary scattering may contribute more significantly to the Hall effect measurements in the undoped samples with smaller grains. In contrast, the larger grain sizes in substituted samples reduce the influence of grain boundaries, likely providing more reliable carrier concentration values. The carrier concentration follows a trend similar to S' values, increasing up to $x = 0.10$ and then decreasing for higher x. We believe that at a certain level of Sm content, the density of thermally activated carriers becomes more significant than that of extrinsic carriers from impurities. To further understand the impact of Sm substitution, we applied the Pisarenko relation at 300 K, analyzing the relationship between the Seebeck coefficient (S) and the carrier concentration (n_H) to estimate the density-of-states effective mass (m_d^*), as shown in Figure S9(a) (details provided in the Supporting Information). The samples with $x = 0$ to 0.10 closely follow the expected trend based on supplementary equations (S1) and (S2), assuming a constant effective mass. In contrast, the samples with $x = 0.15$ and 0.20 deviate from this trend, most likely due to the influence of the bipolar effect, which alters carrier transport but does not affect the intrinsic band density of states [43]. Although topological effects or magnetic contributions were initially considered as possible influences, no specific features or anomalies related to such phenomena were observed in this study. Therefore, the transport properties can be sufficiently explained using a classical approach based on carrier scattering and phase inhomogeneity.

The temperature-dependent power factor (PF) values for the $Sr_{1-x}Sm_xSi_2$ series are presented in Figure 6(d). A clear enhancement in PF is observed with Sm substitution, increasing from 1.9 mW/m.K^2 at 300 K for undoped $SrSi_2$ to 2.47 mW/m.K^2 for $x =$

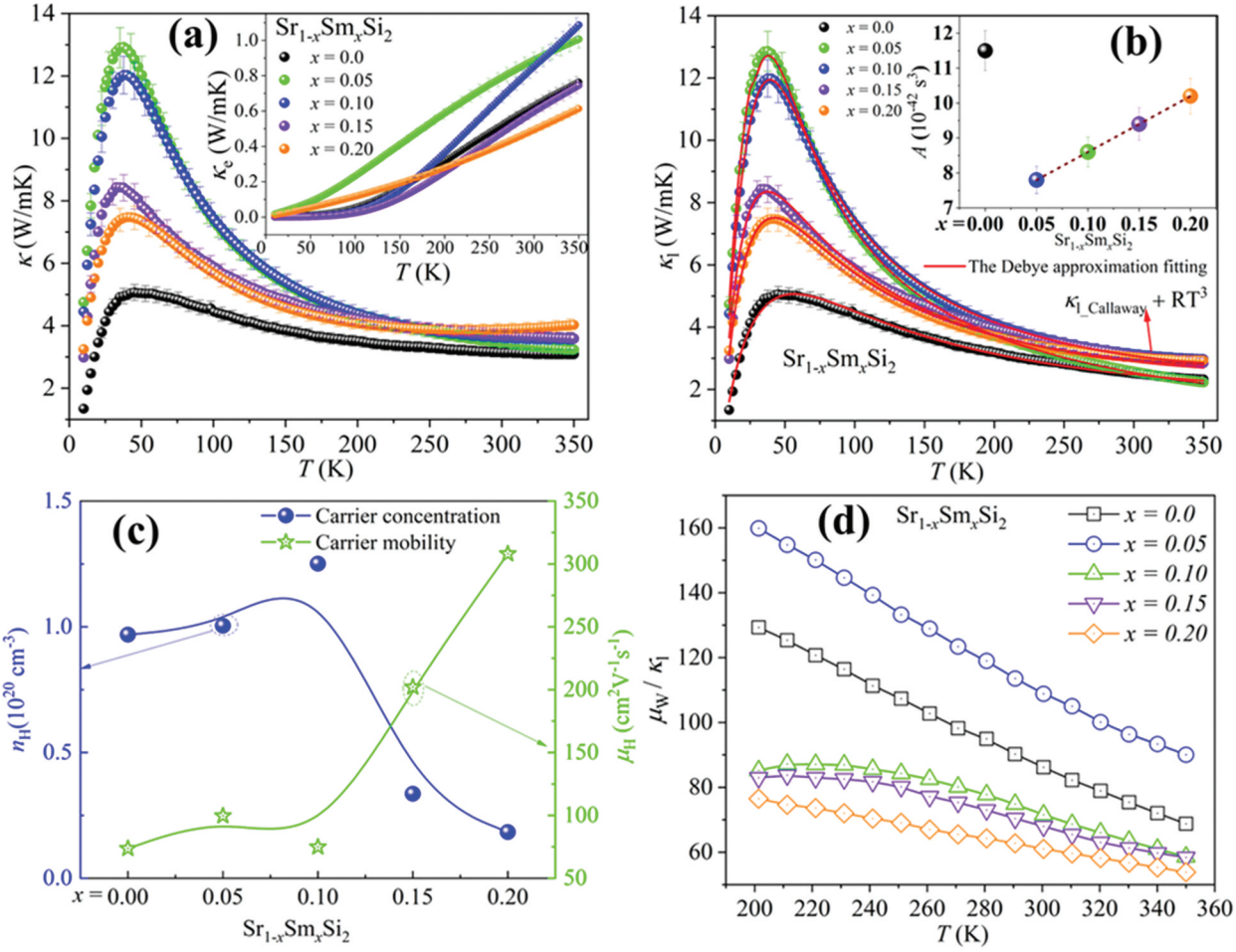

Figure 7. (a) Temperature dependence of the total thermal conductivity $\kappa(T)$ for $Sr_{1-x}Sm_xSi_2$. The inset in (a) shows κ_e, calculated by the Wiedemann – Franz law. (b) Lattice thermal conductivity (κ_l) for $Sr_{1-x}Sm_xSi_2$ as a function of temperature. Each solid curve represents the calculated κ_l using eqs. (4) and (5). The inset shows concentration-dependent point defect scattering parameter A of $Sr_{1-x}Sm_xSi_2$ samples. (c) The carrier mobility and carrier concentration versus Sm content at 300 K, (d) the quality factor μ_W/κ_l of $Sr_{1-x}Sm_xSi_2$.The error bars in Figure (a-b) indicate an estimated uncertainty of ± 5% in the measurements of κ.

0.05. The room temperature *PF* of $Sr_{0.95}Sm_{0.05}Si_2$ is higher than those reported in previous studies on $SrSi_2$ (see Figure S7(b)) [15,19,31,32,44]. Additionally, the $Sr_{0.95}Sm_{0.05}Si_2$ composition exhibits a peak *PF* of 2.9 mW/m.K^2 at approximately 200 K, marking a more than 50% improvement compared to the peak *PF* of undoped $SrSi_2$. In addition, these values are competitive with several established *p*-type silicides [45], half-Heusler, antimonides, and chalcogenides thermoelectric materials at the same temperature range [46]. In our PPMS system measurements, the typical error margin for the Power Factor (*PF*) is estimated to be around 15%, as previously mentioned for electrical resistivity and Seebeck coefficient measurements. These uncertainties affect *PF* calculation and arise from several factors, including instrumental precision, sample geometry measurements, and contact resistance [47,48].

Next, we calculated the $Sr_{1-x}Sm_xSi_2$ samples' weighted mobility (μ_w) in the 200–350 K temperature range using our experimental data (Figure S8(a)). Snyder et al. [49] proposed an empirical equation to calculate weighted mobility from the Seebeck coefficient and electrical resistivity as follows:

$$\mu_w = 331\frac{cm^2}{Vs}\frac{m\Omega cm}{\rho}\left(\frac{T}{300K}\right)^{-3/2}\left[\frac{exp\left[\frac{|S|}{k_B\backslash e}-2\right]}{1+exp\left[-5\left(\frac{|S|}{k_B\backslash e}-1\right)\right]}\right] + \left[\frac{\frac{3}{\pi^2}\frac{|S|}{k_B\backslash e}}{1+exp\left[5\left(\frac{|S|}{k_B\backslash e}-1\right)\right]}\right] \quad (2)$$

The present samples exhibit high-weighted mobilities of ~210 cm^2/V·s for undoped $SrSi_2$ and ~285 cm^2/V·s for $Sr_{0.95}Sm_{0.05}Si_2$ at room temperature, which is notably high compared to other thermoelectric materials, as shown in Figure S8(b). For instance, Bi_2Te_3 alloys typically exhibit μ_w values of 200–300 cm^2/V·s, while PbTe demonstrates μ_w around 100–200 cm^2/V·s [49,50]. Such a high μ_w highlights the superior electronic transport properties of the Sm-substituted $SrSi_2$

system, making it a competitive candidate for thermoelectric applications.

3.2.3. Thermal conductivity

The temperature dependence of the total thermal conductivity κ, the electronic thermal conductivity κ_e, and the lattice thermal conductivity κ_l are shown in Figure 7. The thermal conductivities of $Sr_{1-x}Sm_xSi_2$ samples are 3.2–3.7 W/m.K at 300 K (Figure 7(a)). The current samples showed lower room temperature thermal conductivities than those reported by R. Ghannam et al. [19], and Singh et al. [15], who also utilized the SPS process to fabricate their samples. At low temperatures, κ rises with temperature, peaking at 20–40 K due to phonon scattering from point defects. A notable trend in κ is the drastic reduction in the height of the low-temperature peak with increasing Sm substitution, indicating enhanced phonon scattering. The undoped $SrSi_2$ sample exhibits the lowest κ at low temperatures and a diminished phonon peak, attributed to Sr deficiency, confirmed by SEM/EDS analysis. This deficiency enhances phonon scattering by lattice imperfections, similar to trends also shown by Lue et al. [41]. The κ of the $Sr_{1-x}Sm_xSi_2$ samples showed an increasing trend from 250 to 350 K, which is attributed to the bipolar diffusion effect. A dip in the κ data of $Sr_{1-x}Sm_xSi_2$ samples was observed at 223 K, followed by an increase at higher temperatures. We consider the coexistence of holes and electrons with comparable concentrations. The bipolar diffusion effect was noticed earlier in narrow-band gap systems [51–53]. As Sm substitution in $SrSi_2$ introduces an additional electron, it alters the concentration of majority carriers (details in ESI file).

κ_e was calculated by the Wiedemann–Franz law, $\kappa_e = LT/\rho$, where L is the Lorenz number. For a degenerate semiconductor, L can be estimated from S data using the empirical relation [54]:

$$L = 1.5 + exp\left[\frac{|S|}{116}\right] \quad (3)$$

where S is in μV/K. The calculated value of L increases monotonically with temperature. The L value ranges from 1.81×10^{-8} to 2.05×10^{-8} WΩ/K^2. The electronic part (κ_e) increased with Sm content at 0.05 and 0.1, then decreased for $x = 0.15$ and 0.2, following the same trend as electrical resistivity.

The lattice thermal conductivity, κ_l, is obtained by subtracting κ_e from the total thermal conductivity, and the result is presented in Figure 7(b). To clarify the origin of the significant reduction of κ_l in $Sr_{1-x}Sm_xSi_2$, we fitted the experimental κ_l data by using the Debye-Callaway approximation [55]:

$$\kappa_l = \frac{k_B}{2\pi^2 v_s}\left(\frac{k_B T}{\hbar}\right)^3 \int_0^{\frac{\theta_D}{T}} \frac{x^4 e^y}{\tau_p^{-1}\left[e^y - 1\right]^2} dy \quad (4)$$

Here, $y = {}^{\hbar\omega}/_{k_B T}$ is a dimensionless quantity in which ω, $\hbar$, k_B, θ_D, v_s, and τ_p are the phonon frequency, reduced Planck constant, the Boltzmann constant, the Debye temperature, the average phonon velocity, and the phonon scattering relaxation rate, respectively. The relaxation rate is described as [56]:

$$\tau_p^{-1} = \frac{v_s}{l} + A\omega^4 + B\omega^2 T exp\left(-\frac{\theta_D}{3T}\right) \quad (5)$$

The terms on the right-hand side of Equation 5 refer to scattering on grain boundaries with average grain size l, point defects, and phonon Umklapp processes, respectively. A and B are material-dependent constants. The least-squares fit results from Equations 4 and 5 are shown as solid lines in Figure 7(b). As suggested by Pope et al. [57], a term RT^3, with R being a fitting parameter, can be added to the least squares fit model as a correction to account for radiation losses at temperatures above 200 K, which inherently arise for steady-state measurement setups, as discussed in [27] essential to the steady state heat flow technique, there is a good agreement between the experimental and theoretical results. There is no single solution for fitting the model; a range of parameter sets can provide a reasonable fit. However, a thorough analysis reveals that the value of R is clearly defined and fluctuates by less than 1% across all the different solutions of the model. This indicates that the T^3 correction is valid and should result in only minor errors. Additionally, incorporating the radiation loss term RT^3, without altering the already refined parameters, improves the fitting near 300 K.

In general, grain-boundary scattering dominates at low temperatures, while the Umklapp process is significant at high temperatures. Point-defect scattering also notably affects the shape and position of the phonon peak in the mid-temperature range. The low-temperature peak in κ_l is highly sensitive to different mechanisms of phonon scattering in crystalline solids. The parameters obtained from these least-squares fits are tabulated in Table 3. The higher grain-boundary scattering value (v_s/l) in the undoped $SrSi_2$ aligns with the smaller grain sizes observed in the EBSD analysis. However, the lack of a systematic trend in the v_s/l values with increasing Sm content suggests that other factors in phonon scattering mechanisms may also play a role in influencing these values [31,56,58]. Moreover, KAM mapping and grain boundary misorientation shown in Figure 5 identify local strain and deformation, correlating it with defect-induced phonon scattering. Higher KAM values often indicate increased defect density, which is beneficial for reducing κ_l in thermoelectric materials.

The point defect scattering parameter A (associated with the phonon scattering rate $A\left(\tau_p^{-1} \propto A\omega^4\right)$) exhibits its highest value of 11.5 in the undoped $SrSi_2$ sample. This is likely attributed to Sr deficiency, as confirmed by EDS analysis, which enhances point defect scattering and leads to suppression of the phonon peak, consistent with previous findings in Sr-deficient alloys reported by Lue et al. [59]. The synthesis of the $SrSi_2$ system faces challenges due to Sr deficiency caused by inherent volatility, even with a 5% excess.

Upon Sm substitution, the A value initially decreases, reaching 7.8 for $x = 0.05$, indicating a reduction in point defect scattering. This trend indicates that low levels of Sm incorporation contribute to stabilizing the lattice by reducing Sr volatility and minimizing vacancy formation. This is further supported by the improved compositional homogeneity shown in Table 1, as well as by previous studies that demonstrate enhanced structural stability and decreased vacancy formation resulting from cationic doping [60–62].

However, with further Sm substitution, the A parameter shows a gradual increase, rising to 10.2 at $x = 0.20$ (Table 3). This behavior may be attributed to the onset of additional phonon scattering arising from mass fluctuation and local lattice strain induced by higher Sm content. These results indicate a delicate balance: while initial Sm substitution compensates for intrinsic structural deficiencies, excessive substitution introduces new scattering sources, influencing the overall phonon transport.

The efficiency of point defect scattering arises from the combined effects of mass fluctuations and volume variances of atoms. In general, this efficiency can be quantified using a disorder parameter Γ, expressed as $\Gamma = \Gamma_m + \Gamma_s$, where the subscripts m and s represent mass and strain field, respectively. The disorder parameter Γ for $Sr_{1-x}Sm_xSi_2$ samples was estimated following the method described in Ref [63], and the data for relative atomic mass and covalent radius were obtained from Ref [64]. Figure S7(a) shows that as the Sm content increases, the strain field fluctuations (Γ_s) have a limited effect because of the relatively smaller covalent radius differences between Sr ($R_{Sr} = 1.95$ Å) and Sm ($R_{Sm} = 1.98$ Å). On the other hand, the mass fluctuations (Γ_m) have a more significant effect on lowering κ_l due to the more considerable mass difference between them ($M_{Sr} = 87.52$ and $M_{Sm} = 150.36$). This observation highlights the importance of point-defect scattering in the lattice thermal conductivity of substituted $SrSi_2$ alloys. However, we did not observe any systematic changes in the Umklapp coefficient B from our fits. We conclude that the variation in lattice thermal conductivity at low temperatures in these alkaline-earth-metal silicides is likely due to modifications in the point-defect scattering mechanism.

Table 3. Parameters used to fit the lattice thermal conductivity (κ_l) of $Sr_{1-x}Sm_xSi_2$.

$Sr_{1-x}Sm_xSi_2$	v_s/l (10^9 s^{-1})	A (10^{42} s^3)	B (10^{-17} $s.K^{-1}$)
$x = 0$	1.48	11.5	1.26
$x = 0.05$	1.11	7.8	1.62
$x = 0.10$	0.86	8.6	1.36
$x = 0.15$	1.05	9.4	2.1
$x = 0.20$	0.98	10.2	1.9

The quality factor μ_W/κ_l, which is the ratio of weighted mobility and lattice thermal conductivity, serves as a reliable indicator of thermoelectric performance [65]. High-weighted mobility and low lattice thermal conductivity are essential to achieving outstanding thermoelectric performance. The calculated values of μ_W/κ_l are shown in Figure 7(d). At room temperature, the μ_W/κ_l of $Sr_{0.95}Sm_{0.05}Si_2$ exhibits a substantial increase of ~ 60% compared with that of undoped $SrSi_2$. This increase illustrates the strategic tailoring of scattering centers to reduce lattice thermal conductivity and enhance carrier mobilities. The present μ_W/κ_l ratio for the $Sr_{0.95}Sm_{0.05}Si_2$ sample(~135 at 300 K) is comparable to many well-established high-performance thermoelectric materials near room temperature, such as $(Bi, Sb)_2(Te, Se)_3$, $Mg_3(Sb, Bi)_2$, MgAgSb, $AgSbTe_2$, Ag_2Se, $CsBi_4Te_6$, and SnSe-based materials, which shows values around 100–150 [49,65].

3.2.4. Figure of merit

Figure 8(a) presents the temperature dependence of the ZT value for $Sr_{1-x}Sm_xSi_2$. The ZT_{max} values of about ~ 0.17 and ~ 0.23 for undoped $SrSi_2$ and $Sr_{0.95}Sm_{0.05}Si_2$, respectively, were obtained at 350 K. The ZT value at 300 K for undoped $SrSi_2$ exceeds those reported in $SrSi_2$, as shown in Figure S7(b) [16,31,42]. The approximately 35% improvement in ZT compared to undoped $SrSi_2$ is due to an optimized balance between electrical resistivity and the Seebeck coefficient. This balance has been achieved by precisely tuning the Fermi level and suppressing the bipolar effect, even though there is a modest decrease in thermal conductivity. In comparison to other p-type thermoelectric materials, $Sr_{0.95}Sm_{0.05}Si_2$ exhibits competitive performance. For example, p-type ZnSb and $CoSb_3$-skutterudites typically display ZT values of approximately 0.1 to 0.15 and around 0.2 at 300 K, respectively. In contrast, Bi_2Te_3, considered a benchmark thermoelectric material, achieves a ZT of about 1.0 under similar conditions. Although the ZT of $Sr_{0.95}Sm_{0.05}Si_2$ is lower than that of Bi_2Te_3, it presents the advantages of utilizing earth-abundant, non-toxic constituents and scalable synthesis methods. Figure 8(b) compares room temperature ZT and κ_l values for representative p-type TE materials with the present work [66]. These findings position Sm-substituted $SrSi_2$ as a promising candidate for mid-range thermoelectric applications, blending environmental sustainability with cost-efficiency.

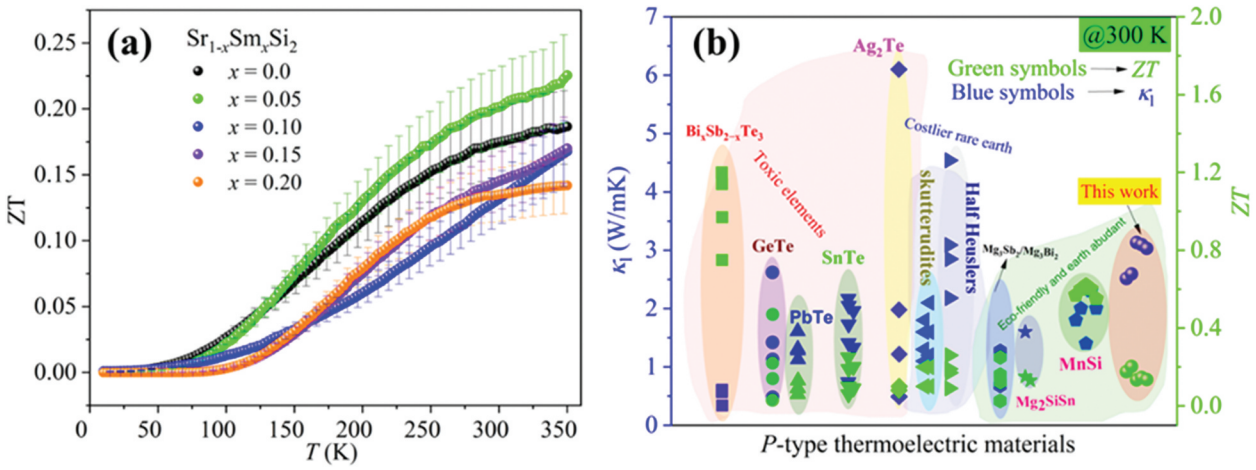

Figure 8. (a) Temperature-dependent Figure of merit *ZT* for the $Sr_{1-x}Sm_xSi_2$ sample. (b) Compare room temperature κ_l and *ZT* values for representative *p*-type TE materials [66]. The uncertainty in the calculated thermoelectric figure of merit (*ZT*) is estimated to be ± 20%, assuming ± 5% errors in κ, *S*, and resistivity (ρ), with negligible contribution from temperature measurement errors.

4. Conclusions

This study systematically investigates the effect of Sm substitution on the thermoelectric properties of $SrSi_2$. The room-temperature electrical resistivity and thermal conductivity show a substantial reduction upon the substitution of Sm ($x < 0.10$) onto the Sr sites of $SrSi_2$. However, the Seebeck coefficients decreased due to substitution ($x < 0.10$). The reduced electrical resistivity and moderate Seebeck coefficient result in a considerably improved power factor. The *PF* of 2.47 mW/m.K^2 observed in $Sr_{0.95}Sm_{0.05}Si_2$ at 300 K is competitive with several established *p*-type thermoelectric materials at room temperature. Moreover, the maximum *PF* of 2.9 mW/m.K^2 at around 200 K for $Sr_{0.95}Sm_{0.05}Si_2$ corresponds to more than 50% enhancement than the peak value for $SrSi_2$. The high *PF* combined with lower thermal conductivity enhances the Figure of merit (*ZT*) in $Sr_{0.95}Sm_{0.05}Si_2$ (*ZT* ~0.23 at 350 K), representing a ~ 35% improvement over pristine $SrSi_2$. Despite these advancements, further reduction in thermal conductivity remains a challenge. Nanostructuring and multiscale defect engineering could further optimize phonon scattering while preserving favorable electronic properties. These findings establish Sm-substituted $SrSi_2$ as a promising and scalable thermoelectric material derived from earth-abundant elements, contributing to the ongoing search for sustainable energy conversion technologies.

Acknowledgments

This work has been supported by the JST Mirai Program, Grant number JPMJMI19A1. The authors express their gratitude to Takanobu Hiroto for his assistance with XRD measurements and to Miwako Takano for her support in SEM observation. VT thanks Tarachand and Rajveer Jha for their support. NT has been supported by JSPS Kakenhi, 24K21692, and 24K00590. The crystal structure of $SrSi_2$ inside Figure 1(b) was drawn with VESTA [67].

Disclosure statement

No potential conflict of interest was reported by the author(s).

Funding

This work was supported by the JST-Mirai Program [JPMJMI19A1]; Japan Society for the Promotion of Science [24K21692]; Japan Society for the Promotion of Science [24K00590].

ORCID

Vikrant Trivedi http://orcid.org/0000-0002-6999-5646
Naohito Tsujii http://orcid.org/0000-0002-6181-5911
Takao Mori http://orcid.org/0000-0003-2682-1846

Data availability statement

Data will be made available on request.

References

[1] Petsagkourakis I, Tybrandt K, Crispin X, et al. Thermoelectric materials and applications for energy harvesting power generation. Sci Technol Adv Mater. 2018;19(1):836–862. doi: 10.1080/14686996.2018.1530938

[2] Rull-Bravo M, Moure A, Fernández JF, et al. Skutterudites as thermoelectric materials: revisited. RSC Adv. 2015;5(52):41653–41667. doi: 10.1039/C5RA03942H

[3] Nolas GS, Slack GA, Morelli DT, et al. The effect of rare earth filling on the lattice thermal conductivity of skutterudites. J Appl Phys. 1996;79(8):4002–4008. doi: 10.1063/1.361828

[4] Sales BC, Mandrus D, Chakoumakos BC, et al. Filled skutterudite antimonides: electron crystals and phonon glasses. Phys Rev B. 1997;56(23):15081–15089. doi: 10.1103/PhysRevB.56.15081
[5] Li A, Wang L, Li J, et al. Global softening to manipulate sound velocity for reliable high-performance MgAgSb thermoelectrics. Energy Environ Sci. 2024;17(22):8810–8819. doi: 10.1039/d4ee03521f
[6] Ohno S, Imasato K, Anand S. Phase boundary mapping to obtain n-type Mg_3Sb_2-based thermoelectrics. Joule. 2018;2(1):141–154. doi: 10.1016/j.joule.2017.11.005
[7] Liu Z, Sato N, Gao W, et al. Demonstration of ultrahigh thermoelectric efficiency of ~7.3% in Mg_3Sb_2/MgAgSb module for low-temperature energy harvesting. Joule. 2021;5(5):1196–1208. doi: 10.1016/j.joule.2021.03.017
[8] Liang Z, Xu C, Song S, et al. Enhanced thermoelectric performance of p-type Mg_3Sb_2 for reliable and low-cost all-Mg_3Sb_2-based thermoelectric low-grade heat recovery. Adv Funct Mater. 2023;33(7):2210016. doi: 10.1002/adfm.202210016
[9] Zhu H, Mao J, Li Y, et al. Discovery of TaFeSb-based half-Heuslers with high thermoelectric performance. Nat Commun. 2019;10(1):1–8. doi: 10.1038/s41467-018-08223-5
[10] Imai M, Naka T, Furubayashi T, et al. Electrical properties of polycrystalline $SrSi_2$. Appl Phys Lett. 2005;86(3):1–3. doi: 10.1063/1.1849423
[11] Shiojiri D, Iida T, Yamaguchi M, et al. Electronic structure tuning of α-$SrSi_2$ by isotropic strain and isoelectronic impurity incorporation: a first-principles study for enhancement of low-temperature thermoelectric performance. J Appl Phys. 2021;130(21):215103. doi: 10.1063/5.0063506
[12] Imai M, Udono H, Alinejad B, et al. Strontium disilicide $SrSi_2$: narrow band gap semiconductor or Weyl semimetal? J Alloys Compd. 2025;1032:181074. doi: 10.1016/j.jallcom.2025.181074
[13] Schierning G. Silicon nanostructures for thermoelectric devices: a review of the current state of the art. Physica Status Solidi (A). 2014;211(6):1235–1249. doi: 10.1002/pssa.201300408
[14] Imai Y, Watanabe A. Calculation of electronic properties of $SrSi_2$ within the framework of a band theory. Intermetallics (Barking). 2006;14(6):666–671. doi: 10.1016/j.intermet.2005.10.010
[15] Singh SK, Imai M. Thermoelectric properties of cubic Ba-substituted strontium disilicide, $Sr_{1-x}Ba_xSi_2$, with Ba content above solid solubility limit. Intermetallics (Barking). 2020;127:106981. doi: 10.1016/j.intermet.2020.106981
[16] Ghannam R, Coulomb L, Moll A, et al. A multiscale approach to enhance the thermoelectric properties of α-$SrSi_2$ through micro-/nano-structuring and Ba substitution. J Alloys Compd. 2024;1002:175422. doi: 10.1016/j.jallcom.2024.175422
[17] Lue CS, Chou MD, Kaurav N, et al. Enhancement in the thermoelectric performance by Y substitution on $SrSi_2$. Appl Phys Lett. 2009;94(19):192105. doi: 10.1063/1.3136847
[18] Shende A, Kore A, Singh P. First-principle based thermoelectric properties of Weyl semi-metal $SrSi_2$. AIP Conf Proc. 2020;2220:130018. doi: 10.1063/5.0001216
[19] Ghannam R, Moll A, Bérardan D, et al. Impact of the nanostructuring on the thermal and thermoelectric properties of α-$SrSi_2$. J Alloys Compd. 2023;968:171876. doi: 10.1016/j.jallcom.2023.171876
[20] Sussardi A, Tanaka T, Khan AU, et al. Enhanced thermoelectric properties of samarium boride. J Materiomics. 2015;1(3):196204. doi: 10.1016/j.jmat.2015.07.007
[21] Sauerschnig P, Tsuchiya K, Tanaka T, et al. On the thermoelectric and magnetic properties, hardness, and crystal structure of the higher boride YbB_{66}. J Alloys Compd. 2020;813:152182. doi: 10.1016/j.jallcom.2019.152182
[22] Sauerschnig P, Vaney JB, Michiue Y, et al. Thermoelectric and magnetic properties of spark plasma sintered REB_{66} (RE = Y, Sm, Ho, Tm, Yb). J Eur Ceram Soc. 2020;40(10):3585–3591. doi: 10.1016/j.jeurceramsoc.2020.03.014
[23] Jaccard D, Sierro J. Valence instabilities. P Wachter and H Boppart, ed. New York: North-Holland; 1982. p. 409.
[24] Ahmed F, Valenta J, Tsujii N, et al. The low and high temperature thermoelectric properties of Yb_3Si_5. Mater Res Express. 2021;8(7):075504. doi: 10.1088/2053-1591/ac128a
[25] Lu F, Zhao J, Weng H, et al. Correlated topological insulators with mixed valence. Phys Rev Lett. 2013;110(9):096401. doi: 10.1103/PhysRevLett.110.096401
[26] Rodríguez-Carvajal J. Recent advances in magnetic structure determination by neutron powder diffraction. Physica B Condens Matter. 1993;192(1--2):55–69. doi: 10.1016/0921-4526(93)90108-I
[27] Tsujii N. Low lattice-thermal conductivity in a cage-structured compound $YbCu_9Sn_4$ with divalent Yb ions. J Alloys Compd. 2014;612:170–175. doi: 10.1016/j.jallcom.2014.05.090
[28] Chen PL, Chen IW. Grain boundary mobility in Y_2O_3 : defect mechanism and dopant effects. J Am Ceramic Soc. 1996;79(7):1801–1809. doi: 10.1111/j.1151-2916.1996.tb07998.x
[29] Yang C, Xiao W, Huang J, et al. Microstructural parameters estimation for sputtered Al coating via SEM, EDS, X-ray diffraction line broadening and EBSD. Vacuum. 2022;206:111496. doi: 10.1016/J.VACUUM.2022.111496
[30] Sun SJ, Tian YZ, Lin HR, et al. Revisiting the role of prestrain history in the mechanical properties of ultrafine-grained CoCrFeMnNi high-entropy alloy. Mater Sci Eng A. 2021;801:140398. doi: 10.1016/j.msea.2020.140398
[31] Kuo YK, Lue CS, Hsu G, et al. Investigation of Al substitution on the thermoelectric properties of $SrSi_2$. Mater Chem Phys. 2012;137(2):604–607. doi: 10.1016/j.matchemphys.2012.10.009
[32] Hashimoto K, Kurosaki K, Imamura Y, et al. Thermoelectric properties of $BaSi_2$, $SrSi_2$, and LaSi. J Appl Phys. 2007;102(6):063703. doi: 10.1063/1.2778747
[33] Natali F, Plank NOV, Ludbrook BM, et al. Epitaxial growth and electrical properties of thick $SmSi_2$ layers on (001) silicon. Jpn J Appl Phys. 2010;49(2R):025505. doi: 10.1143/JJAP.49.025505
[34] Imai Y, Watanabe A. Energetics of alkaline-earth metal silicides calculated using a first-principle pseudopotential method. Intermetallics (Barking). 2002;10(4):333–341. doi: 10.1016/S0966-9795(02)00003-1
[35] Ngugi KJ, Nam WH, Kihoi SK, et al. Detrimental effects of impurity phases on the thermoelectric performance of $Nb_{0.8}Ti_{0.2}Fe_{1.02}Sb$ synthesized by arc-melting. J Alloys Compd. 2021;871:159634. doi: 10.1016/J.JALLCOM.2021.159634

[36] Aoyama K, Shimizu T, Kuramochi H, et al. Enhanced thermoelectric properties of $SrSi_2$ composite films with cubic and layered polymorphs. ACS Appl Energy Mater. 2023;6(12):6593–6597. doi: 10.1021/acsaem.3c00577
[37] Novitskii A, Serhiienko I, Novikov S, et al. Thermoelectric properties of Sm-substituted BiCuSeO oxyselenides fabricated by two-step reactive sintering. J Alloys Compd. 2022;912:165208. doi: 10.1016/j.jallcom.2022.165208
[38] Trivedi V, Tiadi M, Murty BS, et al. Giant thermoelectric efficiency of single-filled skutterudite nanocomposites: role of interface carrier filtering. ACS Appl Mater Interfaces. 2022;14(45):51084–51095. doi: 10.1021/acsami.2c13747
[39] Mao J, Shuai J, Song S, et al. Manipulation of ionized impurity scattering for achieving high thermoelectric performance in n-type Mg_3Sb_2-based materials. Proc Nat acsci. 2017;114(40):10548–10553. doi: 10.1073/pnas.1711725114
[40] Chen ZJ, Tian DB. First-principles calculations of electronic, optical, and thermodynamic properties of $SrSi_2$. J App Phys. 2011;109(3):033506. doi: 10.1063/1.3532031
[41] Lue CS, Wong SF, Huang JY, et al. Chemical pressure effect on thermoelectric properties of Ca and Ba substituted $SrSi_2$ alloys. J Appl Phys. 2013;113(1):013710. doi: 10.1063/1.4772973
[42] Kuo Y-K, Ramachandran B, Lue C-S. Optimization of thermoelectric performance of $SrSi_2$-based alloys via the modification in band structure and phonon-point-defect scattering. Front Chem. 2014;2:120533. doi: 10.3389/fchem.2014.00106
[43] Gong JJ, Hong AJ, Shuai J, et al. Investigation of the bipolar effect in the thermoelectric material $CaMg_2Bi_2$ using a first-principles study. Phys Chem Chem Phys. 2016;18(24):16566–16574. doi: 10.1039/C6CP02057G
[44] Kunioka H, Iida S, Kimura K, et al. Melt growth of crystalline α-$SrSi_2$ by the vertical Bridgman method and its thermoelectric characteristics. J Cryst Growth. 2024;645:127838. doi: 10.1016/j.jcrysgro.2024.127838
[45] Kim G, Shin H, Lee J, et al. A review on silicide-based materials: thermoelectric and mechanical properties. Met Mater Int. 2021;27(7):2205–2219. doi: 10.1007/S12540-020-00609-9
[46] Wolf M, Hinterding R, Feldhoff A. High power factor vs. high zT—a review of thermoelectric materials for high-temperature application. Entropy. 2019;21(11):1058. doi: 10.3390/e21111058
[47] Martin J. Protocols for the high temperature measurement of the Seebeck coefficient in thermoelectric materials. Meas Sci Technol. 2013;24(8):085601. doi: 10.1088/0957-0233/24/8/085601
[48] Borup KA, De Boor J, Wang H, et al. Measuring thermoelectric transport properties of materials. Energy Environ Sci. 2015;8(2):423–435. doi: 10.1039/C4EE01320D
[49] Snyder GJ, Snyder AH, Wood M, et al. Weighted mobility. Adv Mater. 2020;32(25):1–5. doi: 10.1002/adma.202001537
[50] Cho H, Yun JH, Back SY, et al. Superior thermoelectric cooling performance by suppressing bipolar diffusion effect and enhancing anisotropic texture in p-/n-type Bi_2Te_3 based compounds. J Alloys Compd. 2021;888:161572. doi: 10.1016/j.jallcom.2021.161572
[51] Wang S, Yang J, Toll T, et al. Conductivity-limiting bipolar thermal conductivity in semiconductors. Sci Rep. 2015;5(1):10136. doi: 10.1038/srep10136
[52] Kim H, Lee KH, Yoo J, et al. Effect of substitutional Pb doping on bipolar and lattice thermal conductivity in p-type $Bi_{0.48}Sb_{1.52}Te_3$. Materials. 2017;10(7):763. doi: 10.3390/ma10070763
[53] Hauble AK, Toriyama MY, Bartling S, et al. Experiment and theory in concert to unravel the remarkable electronic properties of Na-substituted $Eu_{11}Zn_4Sn_2As_{12}$: a layered Zintl phase. Chem Mater. 2023;35(18):7719–7729. doi: 10.1021/acs.chemmater.3c01509
[54] Kim H-S, Gibbs ZM, Tang Y, et al. Characterization of Lorenz number with Seebeck coefficient measurement. APL Mater. 2015;3(4):041506. doi: 10.1063/1.4908244
[55] Callaway J. Model for lattice thermal conductivity at low temperatures. Phys Rev. 1959;113(4):1046–1051. doi: 10.1103/PhysRev.113.1046
[56] Garmroudi F, Parzer M, Riss A, et al. Pivotal role of carrier scattering for semiconductorlike transport in Fe_2VAl. Phys Rev B. 2023;107(8):L081108. doi: 10.1103/PhysRevB.107.L081108
[57] Pope AL, Zawilski B, Tritt TM. Description of removable sample mount apparatus for rapid thermal conductivity measurements. Cryogenics (guildf). 2001;41(10):725–731. doi: 10.1016/S0011-2275(01)00140-0
[58] Chauhan NS, Zhang Q. Entropy stabilized Heusler alloys for thermoelectric applications. Solid State Sci. 2024;158:107728. doi: 10.1016/J.SOLIDSTATESCIENCES.2024.107728
[59] Lue CS, Tseng YS, Huang JY, et al. Low lattice thermal conductivity suppressed by Sr-deficiency in $Sr_{0.9}Ca_{0.1}Si_2$. AIP Adv. 2013;3(7):072132. doi: 10.1063/1.4817576
[60] Dong J, Sun FH, Tang H, et al. Medium-temperature thermoelectric GeTe: vacancy suppression and band structure engineering leading to high performance. Energy Environ Sci. 2019;12(4):1396–1403. doi: 10.1039/C9EE00317G
[61] Wang K, Xiang H, Xu L, et al. The effect of Nb doping on the properties of Ti-Al intermetallic compounds using first-principles calculations. Materials. 2024;17(2):358. doi: 10.3390/MA17020358
[62] Liu M, Guo M, Lyu H, et al. Doping strategy in metavalently bonded materials for advancing thermoelectric performance. Nat Commun. 2024;15(1):8286. doi: 10.1038/s41467-024-52645-3
[63] Garmroudi F, Parzer M, Riss A, et al. Solubility limit and annealing effects on the microstructure & thermoelectric properties of $Fe_2V_{1-x}Ta_xAl_{1-y}Si_y$ Heusler compounds. Acta Mater. 2021;212:116867. doi: 10.1016/j.actamat.2021.116867
[64] Atomic Radius | Periodic Table of Elements – PubChem. Available from: https://pubchem.ncbi.nlm.nih.gov/ptable/atomic-radius/
[65] Zhu Y, Yu Y, Zhang H, et al. Large mobility enables higher thermoelectric cooling and power generation performance in n-type $AgPb_{18+x}SbTe_{20}$ crystals. J Am Chem Soc. 2023;145(45):24931–24939. doi: 10.1021/jacs.3c09655
[66] Freer R, Ekren D, Ghosh T, et al. Key properties of inorganic thermoelectric materials—tables (version 1). J Phys Energy. 2022;4(2):022002. doi: 10.1088/2515-7655/ac49dc
[67] Momma K, Izumi F. *VESTA 3* for three-dimensional visualization of crystal, volumetric and morphology data. J Appl Crystallogr. 2011;44(6):1272–1276. doi: 10.1107/S0021889811038970